The impacts of 3D radiative transfer effects on cloud radiative property simulations and retrievals

CyberTraining: Big Data + High-Performance Computing + Atmospheric Sciences

Yunwei Cui[1], Meng Gao[2], Scott Hottovy[3],
Research assistant: Chamara Rajapakshe[2],
Faculty mentor: Zhibo Zhang[2]

[1]Department of Mathematics and Statistics, Towson University
[2]Department of Physics, UMBC
[3]Department of Mathematics, US Naval Academy

Technical Report HPCF–2018–15, hpcf.umbc.edu > Publications

Abstract

Satellite observations provide good opportunities to evaluate global cloud system, but the 3D effects induced by the horizontal inhomogeneity of the medium also cause possible uncertainties in the cloud products. In this work, we evaluated the MODIS cloud observations and generated the surrogate cloud using the inverse 2D Fourier transform of synthetic matrices. Both the 3D and 1D radiative transfer simulation studies are conducted in order to understand the impacts of the 3D effects. We retrieve the cloud optical thickness(COT) and cloud effective radius(CER) from the simulated reflectance at 0.86μm and 2.1μm bands and compare between the retrieval and true values. The impacts in the cloud liquid water path retrieval are further studied and we find that the bias in the COT and CER will cause the over estimation of the liquid water path(LWP) estimations for both the illuminating and shadowy pixels.

1 Introduction

Satellites have revolutionized human being's ability to observe the earth and its climate system. Besides offering a global perspective, satellite remote sensors can provide higher spatial and temporal coverage that otherwise would not be possible. Satellite observations also provide a rich variety of atmospheric data records, due to its ability to collect data across a wide range of wavebands of the electromagnetic spectrum, including those beyond the visible lights.

To generate useful data for quantitative analysis, proper retrieval model and algorithm need to be developed to process the products of different sensors. In most atmospheric research, the current radiative transfer models and remote sensing algorithm are based on the one-dimensional (1D) plane-parallel atmosphere model [7, 8]. In this model, the medium is assumed to be horizontally homogeneous and as a results there is no net horizontal photon transport. The 1D radiative transfer model is a reasonable approximation when the horizontal variability of the medium is small. However, some medium, such as cloud fields, have significant horizontal variability. For example, cumulus cloud fields with a wide range of horizontal variability are shown in figure 1.1 (from [12]). These four cloud scenes have

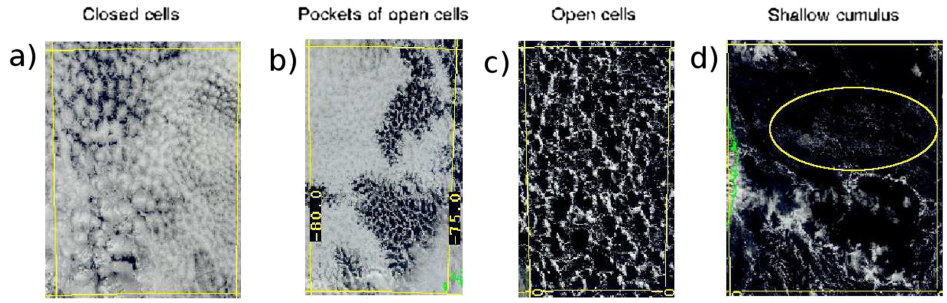

Figure 1.1: Figure from [12]. The figure shows the rich variety of shallow cumulus clouds and its complex two dimensional structure.

vastly different impacts on radiative transfer. Closed cells (panel (a)) reflect most of the sun's radiation, while shallow cumulus (panel (d)) reflect almost none. Pockets of open cells (panel (b)) and open cells (panel (c)) will have a variable effect depending on the different length scales associated with them.

As a result, the 1D radiative theory may cause bias in interpreting the satellite measurement. Applying 1D radiative transfer theory in such cases without any correction could lead to substantial error in satellite retrievals for certain solar and viewing geometries. For example, at the low solar zenith angle the so-called illuminating and shadowing effects can significantly bias the 1D radiative transfer based cloud property retrievals.

The problem has attracted considerable interest among researchers. Várnai and Marshak [13] proposed a method combining visible (0.86 μm) and thermal infrared (11 μm) images to see whether 3D radiative effects make clouds appear asymmetric. Based on the analysis of optical thickness retrievals for real cloud scenes (granules), they found out that 3D cloud heterogeneities have a complicated impact on the retrievals of cloud properties and 3D radiative effects occur quite frequently. Marshak et al. [6] investigated the effects of horizontal inhomogeneity on the retrievals of cloud droplet sizes. They found that the droplet sizes could be underestimated or overestimated, depending on the pixel scale. Seethala and Horváth [1] compared Advanced Microwave Scanning RadiometerEOS (AMSRE), Wentz, and Moderate Resolution Imaging Spectroradiometer (MODIS) cloud liquid water path estimates in warm marine clouds. They found that MODIS showed strong overestimations at high latitudes and the cloud type also affects the bias. Grosvenor and Wood [4] used observation data to investigate MODIS satellite retrieval biases of the cloud optical thickness and the cloud top effective radiums that occur at high solar zenith angles and how they affect retrievals of cloud droplet concentration. A simulation study was also used to investigate the effects of drizzle and cloud horizontal inhomogeneity on cloud effective radius retrievals from MODIS. Using synthetic cloud fields from a large-eddy simulation (LES) model as input to drive 3D radiative transfer models to simulate satellite observations, Zhang et al. [15] compared the retrieved cloud property with the original simulated cloud field to identify the influence of various factors on passive cloud property retrievals.

This project is concerned with the simulation study of the 3D radiative transfer effects

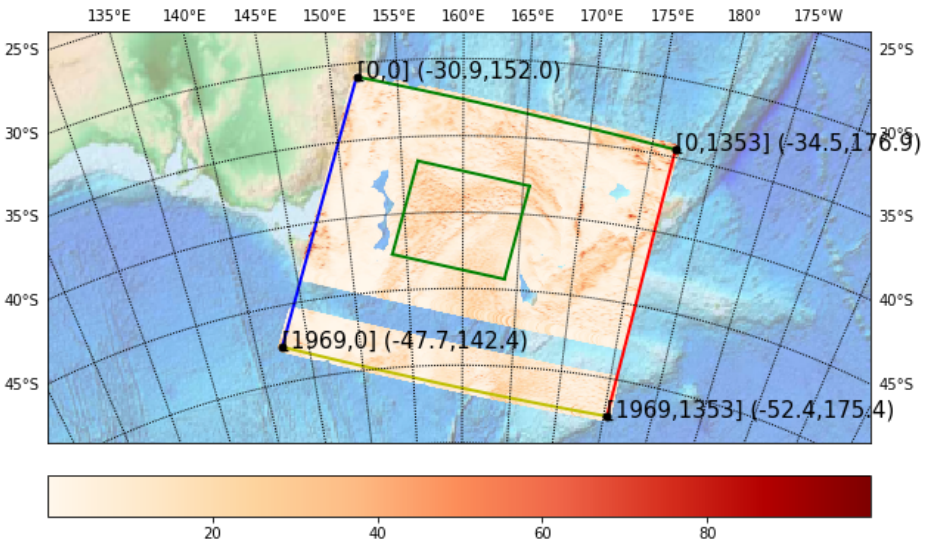

Figure 2.1: Central region of the granule MOD06_L2.A2000306.2325.006.2014297154828.hdf

on cloud radiative properties. Section 2 describes how cloud statistics of observation data were retrieved from MODIS data. Section 3 describes how the power spectral density (Section 3.1) is used to generate the cloud models in one spatial dimension (Section 3.2) and two spatial dimensions (Section 3.3). For the 2D model, the PSD of MODIS data is fed into a surrogate cloud model to generate cloud fields with similar features. Section 4 describes the Spherical Harmonics Discrete Ordinate Method (SHDOM) and how it was used to simulate the radiative transfer model. The COT, CER, and LWP were retrieved and compared for the illuminated and shadowy pixels in Section 5. The conclusions are summarized in Section 6.

2 Statistics of MODIS

MODIS offers unique opportunities to retrieve features of the cloud files because of its excellent radiometric performance (Várnai and Marshak, 2002). Figure 2.1 shows the central region of a granule on March 6, 2000 from the Terra satellite. When we retrieve the COT and CER, we selected the granules which are over the ocean. Each pixel of the granule file represents a 1km by 1km region. As in Várnai and Marshak (2002) [13], we investigated the cloud scenes of size 50km by 50km. Due to various technical reasons, many COT and CER values are missing. We surveyed the 50km×50km regions on the selected granule file, and only kept the regions without any missing values.

Cloud top height is added to the MODIS data using the method described in Section 3.3.1. This gives MODIS derived data for COT, CER, and cloud top height.

3 Cloud Field Models

In this section, cloud field models are defined and developed for both one and two horizontally spatial variables. That is, the cloud optical thickness (COT) τ, is defined at every point in one spatial dimension $\tau(x)$ (here referred to as 1D) and two spatial dimensions, $\tau(x, y)$ (here referred to as 2D).

3.1 Power Spectral Density

The statistic that we study is the power spectral density. The power spectral density is defined as the square of the magnitude of the Fourier coefficients of the signal. For example, if the cloud optical thickness $\tau(x)$, is defined at points x_i for $i = 0, 1, 2, ..., N-1$, then the discrete Fourier transform (DFT) is defined as

$$\hat{\tau}(k) = \sum_{i=0}^{N-1} e^{-2\pi\hat{i}ik/N}\tau(x_i), \tag{3.1}$$

where $\hat{i}$ is the complex number. The inverse DFT is defined as

$$\tau(x_i) = \frac{1}{2\pi}\sum_{k=0}^{N-1} e^{2\pi\hat{i}ik/N}\hat{\tau}(k). \tag{3.2}$$

Thus the power spectral density, $P_\tau(k)$ is defined as

$$P_\tau(k) = |\hat{\tau}(k)|^2. \tag{3.3}$$

The power spectral density shows which wave lengths have the most energy. Note that if we define

$$\text{Total Energy} = \sum_{i=0}^{N-1} |\tau(x_i)|^2, \tag{3.4}$$

then by Parseval's theorem

$$\text{Total Energy} = \sum_{i=0}^{N-1} |\tau(x_i)|^2 = \sum_{k=0}^{N-1} |\hat{\tau}(k)|^2 = \sum_{k=0}^{N-1} P_\tau(k). \tag{3.5}$$

Hence the name, power spectral density.

The above definitions hold in two dimensions by taking the Fourier transform in x and then y. That is,

$$\hat{\tau}(k_x, k_y) = \sum_{i=0}^{N-1}\sum_{j=0}^{M-1} \tau(x_i, y_j)e^{2\pi\hat{i}(ik_x/N + jk_y/M)}. \tag{3.6}$$

Furthermore, the power spectral density gives information about the correlation lengths of τ. This follows from the DFT, that is,

$$P_\tau(k) = |\hat{\tau}(k)|^2 = \left(\sum_{i=0}^{N-1} e^{-2\pi\hat{i}ik/N}\tau(x_i)\right)\left(\sum_{i=0}^{N-1} e^{-2\pi\hat{i}ik/N}\tau(x_i)\right)^* \tag{3.7}$$

$$= \sum_{i=0}^{N-1}\sum_{j=0}^{N-1} \tau(x_i)e^{2\pi\hat{i}ik/N}\tau(x_j)^* e^{-2\pi jk/N} \tag{3.8}$$

$$= \sum_{i=0}^{N-1}\sum_{j=0}^{N-1} \tau(x_i)\tau(x_j)e^{2\pi k\hat{i}(i-j)/N}. \tag{3.9}$$

This expression is similar to the DFT of $\tau(x)\tau(x')^*$. Thus, for a domain of L with resolution L/N, $k = \pm 1$ is the sine wave corresponding to a wavelength L, $k = \pm 2$ is corresponding to wavelength $L/2$, $k = \pm 3$ to $L/3$,..., $k = \pm N/2$ corresponding to a wavelength of $L/(N/2)$.

The variance COT in the cloud scene is contained in the $k_x = k_y = 0$ wave number,

$$\frac{1}{N_x N_y}\sum_i\sum_j \tau(x_i, y_j)^2 = \hat{\tau}(0,0).$$

3.2 1D Synthetic Cloud Generator

In this section, a 1D synthetic cloud generator developed in [2] is studied. The model is called a *bounded cascade* model. The model will generate the cloud optical thickness $\tau(x_i)$ for points, $x_0 = 0,\ x_1 = x_N 2^{-N},\ 2x_N 2^{-N},\ ..., 2^N x_N 2^{-N} = x_N$. Figure 3.1 describes the procedure for the model pictorially.

The assumptions for the model are as follows.

(a) The cloud is plane-parallel with a fixed thickness in the z-direction, and infinite in the y-direction.

(b) The transfer of moisture occurs in a random direction

The model is as follows:

1. Input parameters initial optical thickness τ_{init}, fraction f, order $xorder$.
2. Start with a slab of uniform thickness and distance d km.
3. initialize with a cloud optical thickness of τ_{init}.
4. Divide the slabs, for the nth iteration
   (a) For the ith slab, cut it in half to form two new slabs.
   (b) For each new slab, choose a direction (right/left) at random.

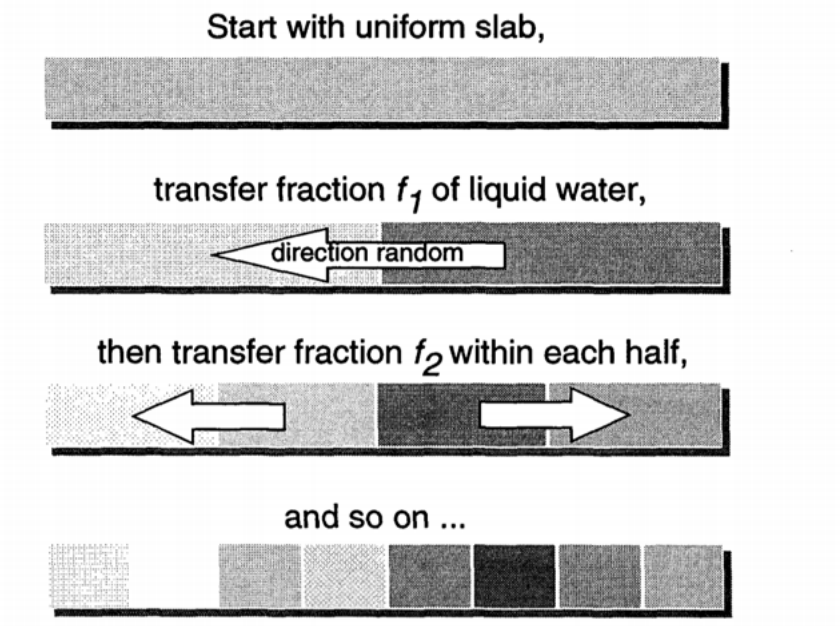

Figure 3.1: Figure from [2]. The figure shows the methodology for generating the 1D fractal cloud optical thickness.

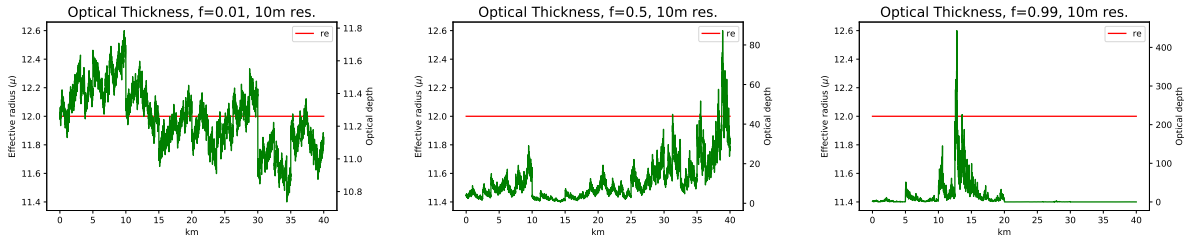

(a) (b) (c)

Figure 3.2: Examples of realizations of the fractal cloud model of [2] for for $\tau_{init} = 12$ and $xorder = 12$ and fraction parameters (a) $f = 0.01$, (b) $f = 0.5$, and (c) $f = 0.99$.

(c) Transfer a fraction $f_n = \frac{f}{2^{n/3}}$ of τ in that direction.

5. Repeat step 4 for $n = xorder$ times.

Some examples of this one dimensional fractal cloud model are shown in figure 3.2. The three panels all have $\tau_{init} = 12$ and $xorder = 12$. However, they differ in their fraction parameters f. In panel (a) only a small fraction of τ is transfered ($f = 0.01$) where as in panel (b) half of the τ is transfered ($f = 0.5$) and in panel (c) almost all of the τ is transfered $f = 0.99$.

Can generalizations of the statistics of the model depending on f be extracted from figure 3.2? From inspection, it could be hypothesized that for small f (panel (a)) the model produces small scale fluctuations across the cloud. For large f (panel (c)) the τ is mostly

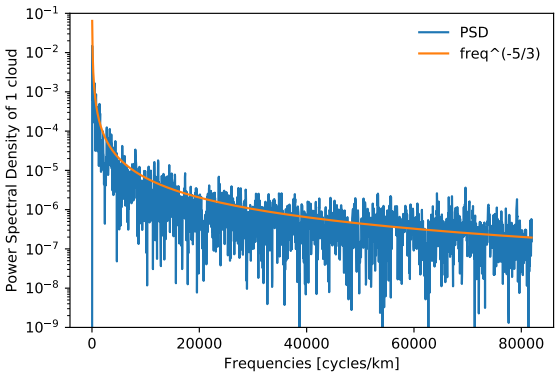

Figure 3.3: The log of the power spectral density of the 1D fractal cloud model for $f = 0.5$, $xorder = 12$, and $d = 1$ km. The solid orange line is a theoretical power law relation ship of $P_\tau(k) = k^{-5/3}$.

located at one position and then decays quickly. For $f = 0.5$ (panel (b)) we see both effects. To quantify this, the power spectral density is computed.

In figure 3.3 the power spectral density is plotted for a realization of the fractal cloud model for $f = 0.5$, $xorder = 12$, and $d = 1$ km. The power spectral density follows a power law of $-5/3$. This is a feature of the model due to the fraction being transfered at each iteration of $f_n = f/2^{n/3}$ where $f = 0.5$. It has been shown that observed cloud fields have a similar power law relationship [3].

To extract the dependence of the model on the inputs $xorder$ and f, many realizations of the model are simulated and an average of the power spectral density is taken. The parameter $d = 1$ km is held fixed as it only controls the resolution of the PSD. That is, $k_{i+1} - k_i = 1/d$.

The results of the sensitivity study are plotted in figure 3.4. In panel (a), the log of the power spectral density is plotted for $xorder = 8$, resulting in a 3 m resolution, and variable f. In panel (a) we see that increasing f leads to more power at all frequencies. Thus for larger f, the fractal cloud will have larger features at the longest wavelengths. Within these long wavelengths, there will also be small fluctuations within. For small f, there is slightly larger power at larger wavelengths but it decays quickly. Thus the result should look similar to white noise (constant along all frequencies). In panel (b), the results for $f = 0.2$ and variable $xorder$ (resolution) are plotted. Here the discrepancies aren't as large as panel (a). Note that larger $xorder$ leads to larger frequencies being sampled. Furthermore, there is slightly larger power for all frequencies. This implies that for smaller resolutions there is more variance for the cloud model.

3.3 2D Surrogate Cloud Generator

The 1D fractal cloud model described above leads to fast simulations and theoretical results for the power spectrum. However, clouds display a rich variety of complex two dimensional

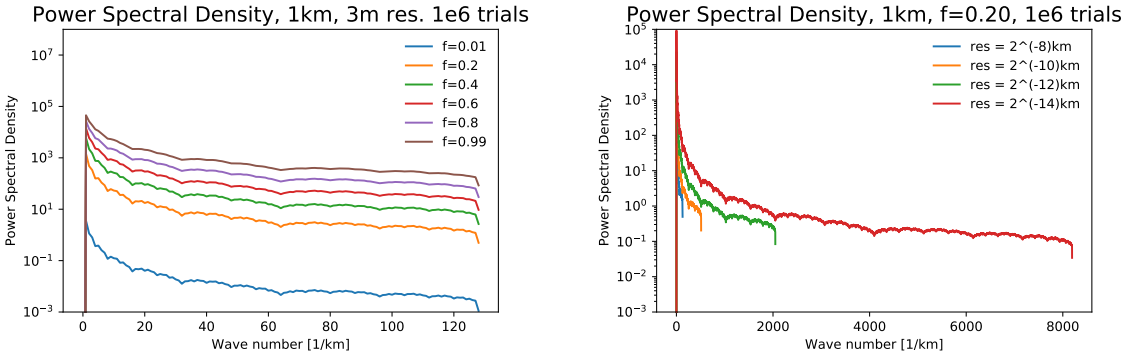

(a) (b)

Figure 3.4: The log of power spectral density of the 1D fractal cloud model with $d = 1$ km, and variable f and $xorder = 8$ (panel (a)), and $f = 0.2$ and variable $xorder$ (panel (b)). Note that the resolution is $2^{-xorder}$ km.

structures (see figure 1.1). Thus a model which captures the two dimension structures of real cloud fields is developed here. This will lead to a testbed of cloud fields, for radiative transfer simulations, which all have the same spatial characteristics as one cloud field. For example, a particular cloud scene, such as panel a) of figure 1.1, can be used to generate many cloud scenes with similar closed cell structures.

The method used here is derived from the paper of [5]. There, the authors describe a *Fourier Cloud Field* as follows:

"Cloud fields were generated by calculating the inverse 2D Fourier transform of synthetic matrices containing wave amplitudes consistent with energy at the various scales indicated by the one dimensional spectrum."

From this paragraph, the following algorithm was used to generate surrogate cloud fields from one observed cloud scene:

1. Remove mean cloud optical thickness τ and store it.
2. Input: Observed Power spectral density (PSD) of τ.
3. Calculate the Fourier coefficients ($\sqrt{PSD}$)
4. Create a random phase shift to generate different cloud fields.
5. Satisfy symmetric condition of the Fourier Transform for real values. For example, in one-dimension, the symmetric condition is

$$\hat{\tau}(-k) = \hat{\tau}(k)^*.$$

6. Take the inverse discrete Fourier transform and add the stored mean.

The algorithm above generates an arbitrary number of different surrogate cloud scenes based on one observed cloud scene. These generated surrogate clouds share similar properties with the original observed cloud scene. Because of the properties of the power spectral density (see Section 3.1) each surrogate cloud field will have the same mean and variance of τ as the original. Further more, the 2D spatial structure in the form of correlations, is preserved.

This method is similar to iterative methods described in [10, 11]. The main difference between those methods and the one described here is the distributions of the surrogate clouds. In [10, 11], the method starts with generating surrogate clouds with linear Gaussian statistics. That is, the probability distribution for the cloud is known exactly. Next the surrogate is changed iteratively, in a way to preserve the distribution, until the statistics are close enough to the original cloud scene. The method described here has no control over the distribution of the cloud scene. Thus, after generating many surrogate clouds for a MODIS cloud scene, the resulting distribution of COT will not be Gaussian. Future work will explore the differences of these methods in more detail.

Three examples of this algorithm are shown in figure 3.5 in columns (a), (b), and (c). The top row are three different cloud scenes from MODIS of the cloud optical thickness τ. The domain of the three scenes are 50km by 50km in the latitude and longitude directions. The three cloud scenes are vastly different in their structures. The cloud scene from (a) has a periodic structure with wavenumber five for $y = 25 - 50$km, where (b) has a large cloud structures in both directions, and (c) has a periodic structure with much larger wavelength and orientated at an oblique angle to the xy axes.

The structures of the MODIS cloud scenes (top row) are captured in the power spectral density plots (PSD) in the middle row of figure 3.5. The PSD shows which length scales are more prominent. The plots are all symmetric about the origin. This is because an oval shaped cloud with its major axis oriented North-East is the same as its major axis oriented South-West. The PSD for cloud scene (a) shows a large amount of power for $k_y = 0$ and $k_x = -5, -4, ..., 4, 5$. This corresponds to the large cloud for all x and $y = 0 - 25$ km ($k_x = \pm 1, \pm 2, \pm 3$), and the periodic structure in $y = 25 - 50$ km ($k_x = \pm 4, \pm 5$). For cloud scene (b), the PSD is roughly radially symmetric for small k_x, k_y. For moderate wave numbers ($k_x, k_y = \pm 10 - 15$) there is a slight oval shape. This is due to the North-East orientation of the clouds. For cloud scene (c), the PSD is strongly oval with a very small semi-minor axis radius. The majority of the power is at wavenumbers $k_x = \pm 10$. This is seen in the MODIS plot with a North-East tilt and periodic structure with roughly 10 peaks.

The algorithm presented above was used to produce the surrogate cloud scenes shown in the bottom row of figure 3.5. All the surrogate clouds have the same PSD as the MODIS clouds (middle row).

3.3.1 Adding cloud thickness and cloud effective radius

The above algorithm generates surrogate clouds given one atmospheric quantity, here that is cloud optical thickness (COT) τ. However, COT, cloud top height (h), and cloud effective radius (CER, r_e) are need to generate statistics from the radiative transfer model (see Section 4). To do so, we use atmospheric relations to derive a crude estimate of cloud top

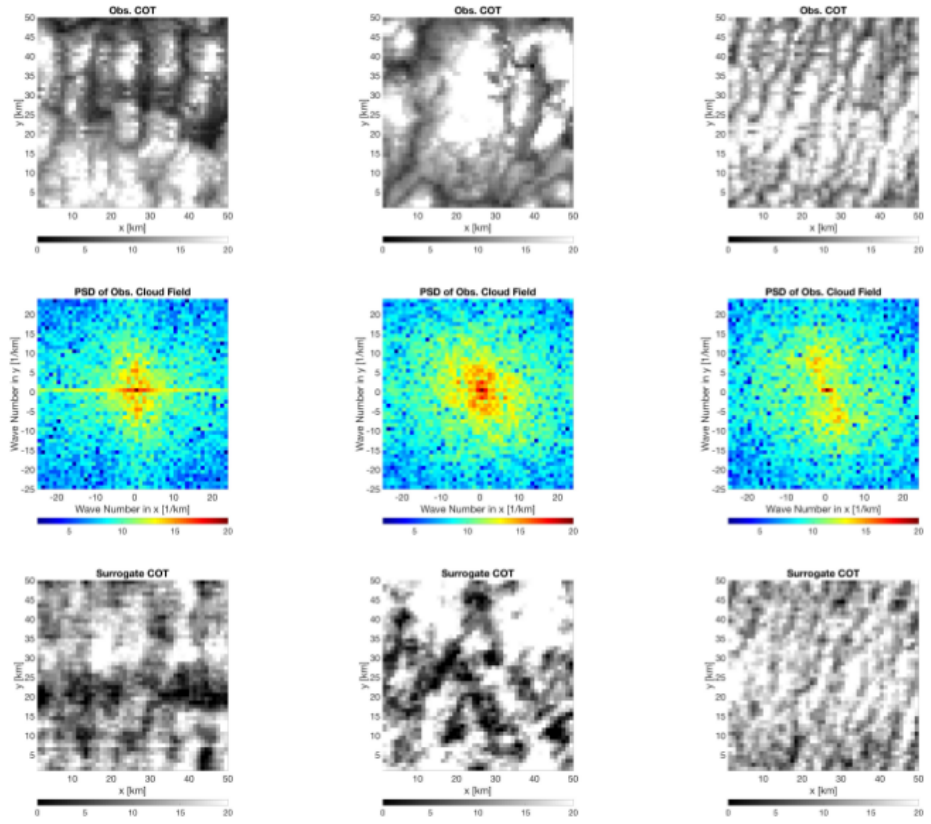

Figure 3.5: The columns (a), (b), and (c) show three examples of clouds scenes with different two dimensional structures. The top row are observed cloud optical thickness, the middle row is the power spectral density of the top row, and the bottom row is the surrogate cloud scene by using the algorithm described in Section 3.3

height and CER [14].

We assume that the liquid water content $q_L(z)$ increases linearly with height z above the cloud base. That is,

$$q_L(z) = f_{ad}\Gamma_{ad}z \tag{3.10}$$

where $0 \leq f_{ad} \leq 1$ is a dimensionless constant which is the degree of adiabaticity, Γ_{ad} is the adiabitic rate of increase of liquid water content with respect to height (in g/(m^3·km). The liquid water path is defined as

$$LWP = \int_0^h q_L(z)dz = \frac{1}{2}f_{ad}\Gamma_{ad}h^2 \tag{3.11}$$

where h is the cloud top height. The cloud optical thickness (dimensionless) is related to the LWP by

$$\tau = \int_0^h \frac{3q_L(z)}{2\rho_w r_e}\, dz, \tag{3.12}$$

where ρ_w is the density of water and r_e is the effective radius of the cloud droplets.

In order to integrate, the vertically varying CER must be expressed in terms of q_L. To do so, we assume that the mean volume radius r_{vol} is defined as

$$r_{vol} = \left(\frac{3q_L}{4\pi\rho_w} N_d \right)^{1/3}, \tag{3.13}$$

where N_d is the droplet concentration. Further more, the fraction of mean volume radius and CER is a constant k. That is,

$$k = \left(\frac{r_{vol}}{r_e} \right)^3. \tag{3.14}$$

Substituting equation (3.13) in for r_{vol} above and solving for r_e. Gives,

$$r_e(z) = \left(\frac{3q_L(z)}{4\pi\rho_w N_d k} \right)^{1/3}. \tag{3.15}$$

Substituting r_e in equation (3.12), integrating, and solving for h yields

$$h = \left(\frac{250^{1/3}\tau\rho_w^{2/3}}{243^{1/3}\pi^{1/3}\Gamma_{eff}^{2/3}N_{eff}^{1/3}} \right)^{3/5}, \tag{3.16}$$

where $\Gamma_{eff} = f_{ad}\Gamma_{ad}$, and $N_{eff} = kN_d$.

To obtain an estimate of CER, we use equation (3.15) and evaluate $z = h$. This gives a value of clout top effective radius.

An example of a cloud scene with cloud effective radius (CER) at cloud top height and cloud top height is shown in figure 3.6. The relations in equations (3.15) and (3.16) for CER and cloud top height to COT respectively were used with the following constants:

$$\rho_w = 997\frac{\text{kg}}{\text{m}^3}, \quad r_e = 12 \cdot 10^{-6}\text{m}, \quad f_{ad} = 1, \quad \Gamma_{ad} = 2.0\frac{\text{g}}{\text{m}^3 \cdot \text{km}}, \quad k = 0.8, \quad N_{eff} = 200\text{m}^{-3}$$

The top row is MODIS retrieved cloud optical thickness (COT) (a) and CER at cloud top height (b). The cloud top height (c) was derived from relation (3.16). The bottom row is from the surrogate model using the power spectral density of MODIS COT. The surrogate COT (a) was generated using the algorithm described above. The CER at cloud top height (b) was generated from COT by using equation (3.15). The cloud top height was generated from COT by using equation (3.16). Note that CER at cloud top height is much smaller for the surrogate model than for MODIS retrieval. This may be due to assumptions made for the relation (3.15).

4 3D Radiative Transfer Models

Satellite observations measures the radiance reflectance of the cloud field where all the 3D effects are observed especially for large solar zenith angle. The cloud properties such as COT,

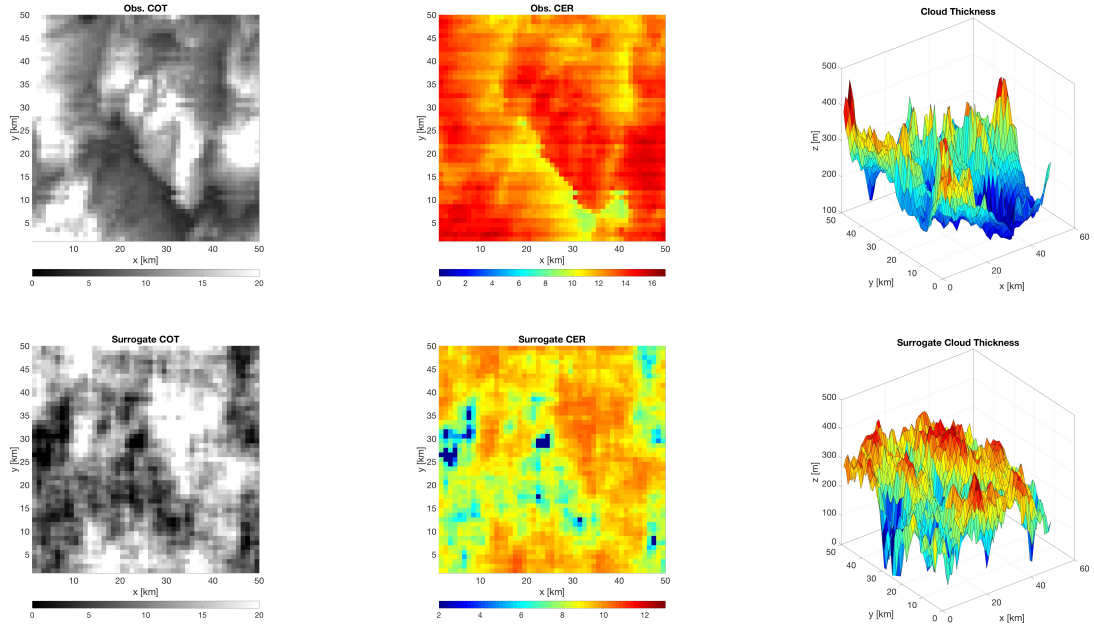

(a) (b) (c)

Figure 3.6: A figure of MODIS retrievals (top row) and the surrogate cloud model (bottom row) of cloud optical thickness τ (column (a)), cloud effective radius at cloud top $r_e(h)$ (column (b)), and cloud top height h (column (c)). For the model, equations (3.15) and (3.16) were used to compute CER and cloud top height, respectively, from COT.

and are usually retrieved from a lookup table based on the Nakajima-King Approach [7, 8] and 1D plane parallel atmospheric system is usually assumed. Through comparing 3D and 1D radiative transfer simulations, we can evaluate the reflectance variation with different cloud structures, and quantify the impact in the COT, CER and LWP retrieval. In order to evaluate such possible impact of the 3D effects, accurate radiative transfer simulations are required. In this study, both the 3D and 1D radiative transfer simulation are conducted using the the Spherical Harmonic Discrete Ordinate Method (SHDOM) developed by Robert Pincus and K. Franklin Evans at University of Colorado, which is widely used and well validated [9].

For the SHDOM simulation, both the cloud geometry and physical properties need to be specified in a 3D grid system and formatted according to the SHDOM input file requirement. The 3D cloud field is generated using the COT, CER and CTH information as discussed in Section 2 and Section 3 on a horizontal domain of 50km by 50km. The grid numbers in x, y, and z are denoted as N_x, N_y and N_z. The choice of the number grids is to balance both good accuracy and minimize the resources.

For each grid point, water droplet size distribution is specified by CER with an assumed variance of 0.1. The single scattering properties includ the phase function and the single scattering albedo are computed using the Lorenz-Mie algorithm through the utility provided by the SHDOM package. Fig 4.2 shows a typical phase function for a cloud droplet size

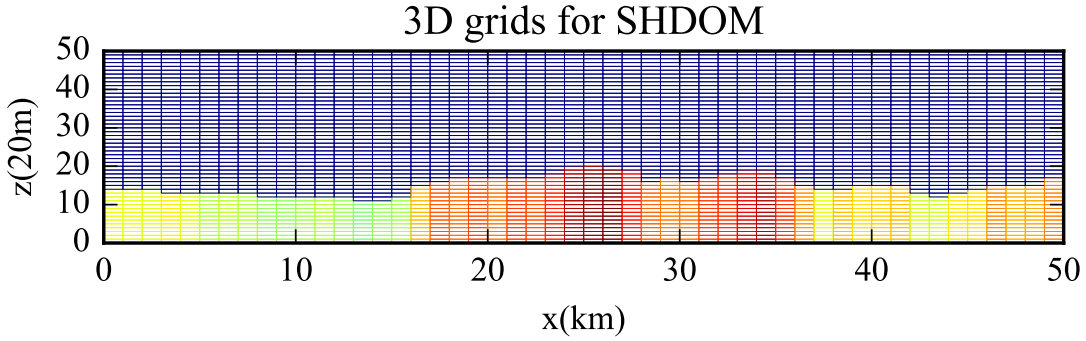

Figure 4.1: Vertical cross section of the computational grids for the 3D SHDOM simulation.

distribution with effective radius of 10μm and variance 0.1 at wavelength 0.75μm. The major features in the phase function including a strong forward scattering peak, an observable backscattering peak, and a prominent rainbow peak around the scattering angle of 140°. To construct the input file, We need to pre-compute the Legendre Polynomial coefficients for the phase function expansion, extinction coefficient, and single scattering albedo. Specifically, the extinction coefficient are determined from the COT and grid spacing. The height of the system z_t is choose as 1km, therefore the grid size is $\Delta z = z_t/n_z$ km. Assuming the height of the cloud is CTH (in our study it is less than 1km), the number of grids contains the cloud would be approximately $n_k = [CTH/z_t \times n_z]$ round as an integer number. The extinction coefficient would be

$$c_e = \frac{COT}{n_k \Delta z} \tag{4.1}$$

$$= \frac{COT}{[CTH/z_t \times n_z] z_t/n_z} \tag{4.2}$$

$$= \frac{COT \times n_z}{[CTH/z_t \times n_z] z_t} \tag{4.3}$$

Note that all the length units are taken as km. A sample vertical cross section of the computational grids is provided in Figure 4.1.

The 3D radiative transfer simulation can be expensive in both the memory and run time cost. SHDOM is a good choice to achieve a reasonable good efficiency when the system is not too large. In order to choose a proper spatial resolution, we valuated the simulation time and memory cost for various grid resolution as summarized in the Tables 4.1 and 4.2. We choose grid size of 50x50x50 to balance both efficiency and accuracy with an approximated radiance accuracy of 2%. Internal adaptive grids are automatically implemented in this study.

Following the Nakajima-King approach as mentioned previously, we generated the COT-CER look up table for different solar zenith angle at two wavelength of 0.86μm and 2.1μm. The COT and CER are then retrieved from the lookup table for both 1D and 3D radiative transfer simulation. We computed the radiance for 7 CER and 15 COT with around 100 cases. The parameters used for the COT and CER retrieval lookup table are summarized

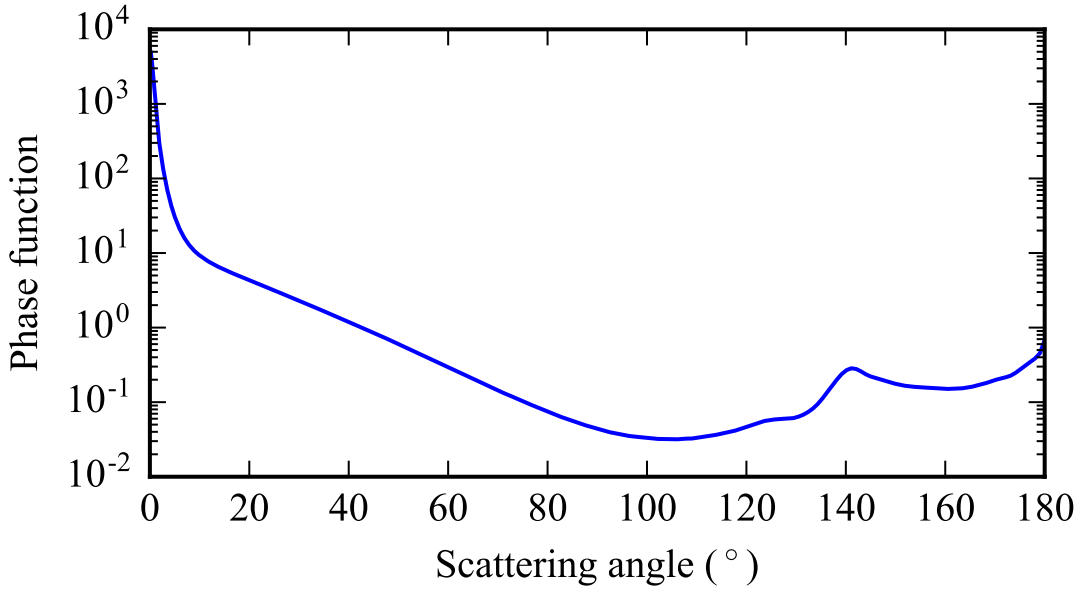

Figure 4.2: Phase function for a cloud droplet size distribution with effective radius of 10um and effective variance 0.1 at wavelength 0.75μm.

Table 4.1: Memory and simulation time cost for 1D SHDOM simulation, with horizontal grids 50 by 50 and various vertical grid number(n_z)

n_z	16	32	50	100
Memory(MB)	86	170	270	529
Time(s/min)	30s	55s	95s	3min

Table 4.2: Memory and simulation time cost for 3D SHDOM simulation, with horizontal grids 50 by 50 and various vertical grid number(n_z):

n_z	16	32	50	100
Memory(MB)	160	320	502	1006
Time(min)	2min	3min	6min	19min

as follows: CER Grids (μm): 5, 10, 15, 20, 25, 30, and 35 ; COT Grids: 0.1, 0.5, 1.0, 1.3, 1.7, 2.2, 3, 4, 5, 7, 10, 15, 20, 25, and 30. The lookup table for three different solar zenith angle are shown in Fig. 4.3. With the measured or the simulated reflectance at the two wavelength, the corresponding COT and CER can be retrieved.

5 Results and Discussions

Following the studies on the cloud optical thickness (COT), cloud effective radius(CER) and cloud top height (CTH) from the MODIS observations as shown in the top panel of

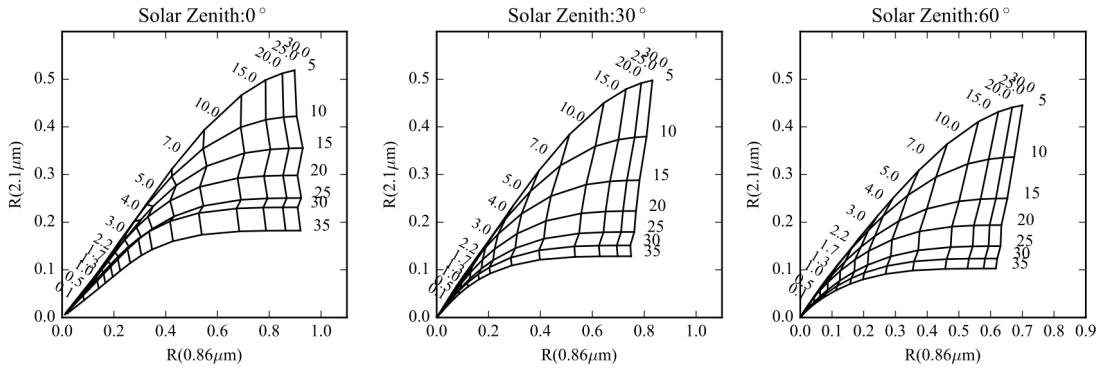

Figure 4.3: COT and CER lookup table for different solar zenith angle of 0°, 30° and 60°.

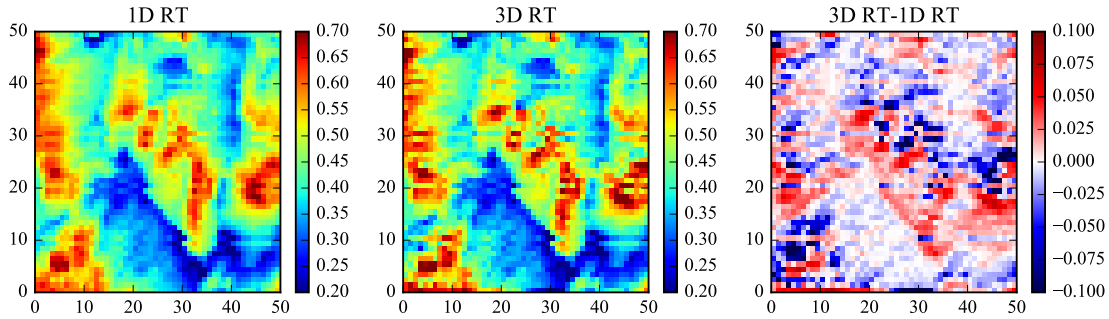

Figure 5.1: The reflectance from the 1D and 3D radiative transfer simulation, and their difference at wavelength of 0.86μm.

Fig 3.6. We construct a 3D cloud model for the SHDOM radiative transfer simulation. The reflectance for both the 1D and 3D simulation are obtained at the two wavelengths of 0.86μm and 2.1μm for a solar zenith angle of 60° as compared in the Figure 5.1 and Figure 5.2. Two types of pixels can be classified in order to understand the 3D effects: the illuminating pixels appears brighter and usually facing toward the sun, and the shadowy pixels appears darker and usually facing away from the sun.

The observed difference in the 1D and 3D radiative transfer simulation results may impact on the COT and CER retrievals and therefore cause bias in the cloud property evaluation. Figures 5.3 and 5.4 shows the comparison of the retrieved COT and CER and the true COT and CER for both 1D and 3D radiative transfer simulation. Since the COT/CER lookup table is constructed from 1D radiative transfer simulation, Figure 5.3 shows good correlation between the retrieved and the true COT and CER. There are still uncertainties in the CER retrieval possibly due to the coarse grids in the lookup table which can improved by using a higher resolution lookup table. However, for the 3D results, Figure 5.4 shows obvious slope difference in the scatter plots, the retrieved COT are different with the true value with both significant over and under estimations. CER retrieval also shows prominent different comparing with the true values.

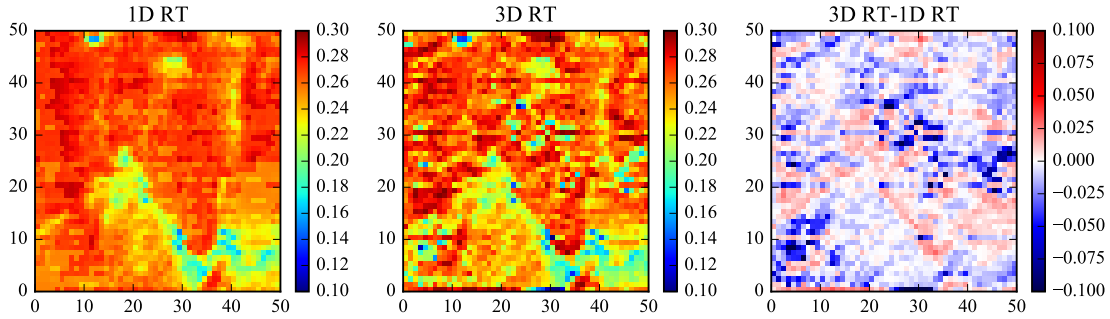

Figure 5.2: The reflectance from the 1D and 3D radiative transfer simulation, and their difference at wavelength of 2.1μm.

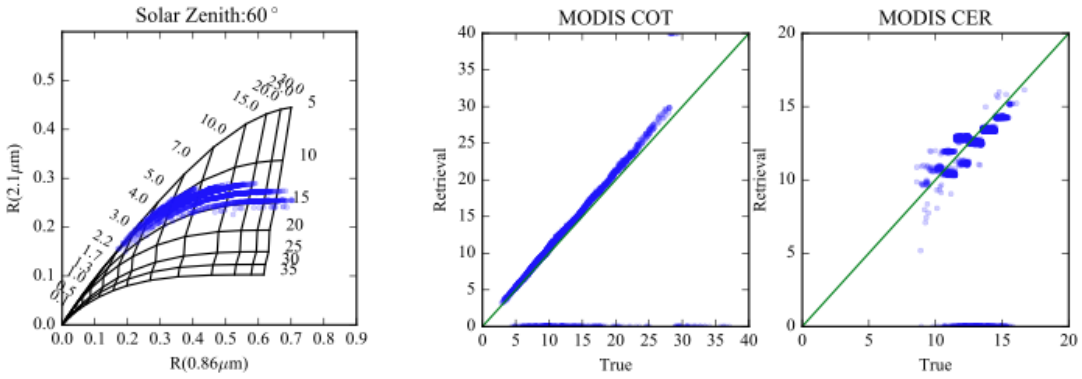

Figure 5.3: The COT and CER retrieval from 1D simulated reflectance. Left panel: the reflectance at the 0.86μm and 2.1μm chanels on the COT CER lookup table plot; Middle panel: the comparison of the true and retrieved COT; Right panel: the comparison of the true and retrieved CER.

In order to understand impact of 3D effects, we separate the retrieval results for the illuminating and shadowy pixels respectively. Furthermore, if the reflectance for both the 0.86μm and 2.1μm have larger 3D simulated reflectance than 1D reflectance, we classified it as the illuminating pixels; if both channels have less reflectance comparing the 3D and 1D reflectance, the pixels are classified as shadowy ones.

For the illuminating pixels, the reflectance from the 3D simulation is larger than the 1D simulation and the retrieved results tend to have larger COT to achieve larger reflectance; while for the shadowy pixels, the retrieved COT tends to be smaller as shown in Figure 5.5. However, the retrieved CER tends to be smaller for the illuminating pixels due to the larger backscattering of a smaller particle size; the retrieved CER tends to be smaller for the shadowy pixels as shown in Figure 5.6.

As discussed by Seethala et al [1], the liquid water path is an important property of the cloud and it is related with the COT and CER as $LWP = 4\rho_w/(3Q_e)COT \times CER$. Therefore the estimated LWP from the satellite observations would directly rely on the accuracy of

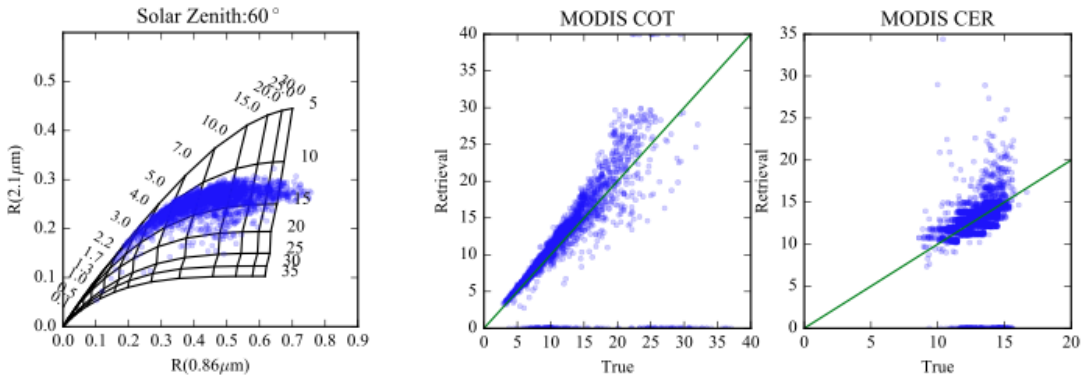

Figure 5.4: The COT and CER retrieval from 3D simulated reflectance. Left panel: the reflectance at the 0.86μm and 2.1μm chanels on the COT CER lookup table plot; Middle panel: the comparison of the true and retrieved COT; Right panel: the comparison of the true and retrieved CER.

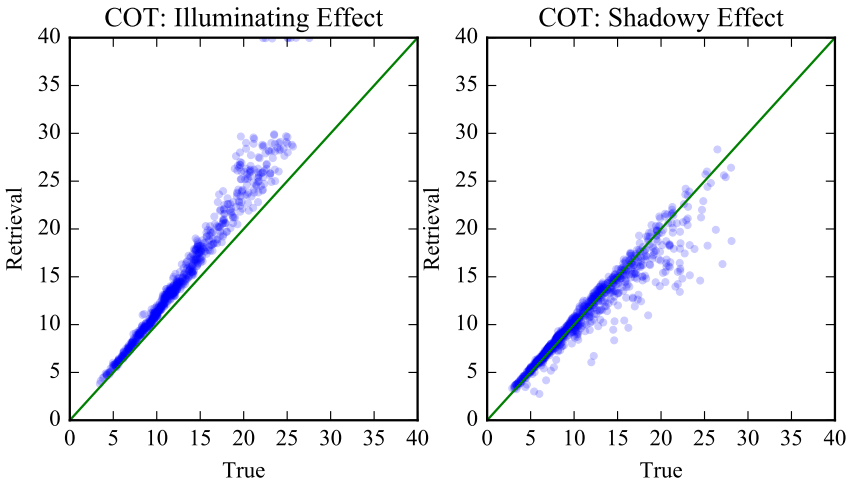

Figure 5.5: The comparison of retireved COT and true values for the illuminating and shadowy pixels.

the retrieved COT and CER. As we have demonstrated for the illuminating pixels, the COT is over estimated while the CER is under estimated, and vice versa for the shadowy pixels. Therefore the effects of COT and CER are compensating each other, and the net effects is the source of the bias in the LWP estimation. In order to evaluate the combined effects of COT and CER, their product are plotted in the Figure 5.7. The retrieved CER*COT are over estimated than the true value for the most illuminating pixels. For the shadowy pixels a majority data points shows over estimation of the CER*COT between the retrieved and the true ones. Therefore in average LWP is over estimated for both shadowy and illuminating pixels.

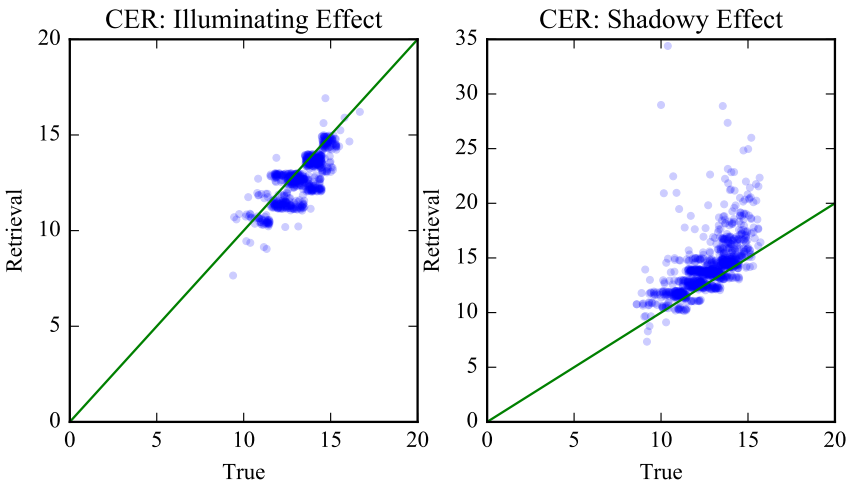

Figure 5.6: The comparison of retireved CER and true values for the illuminating and shadowy pixels.

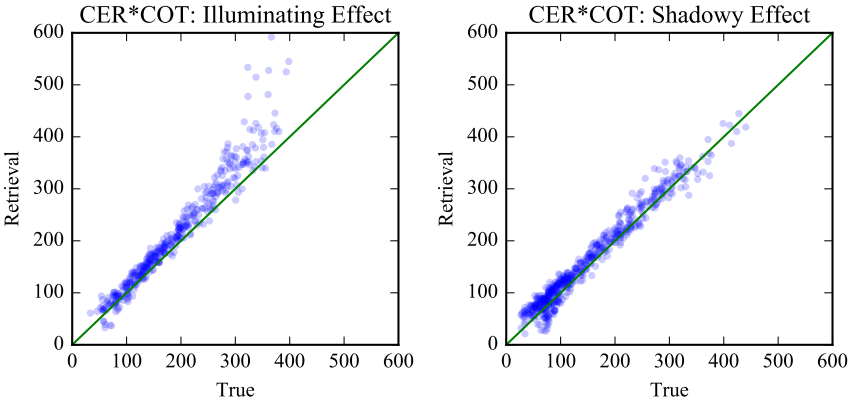

Figure 5.7: The comparison of retireved CER multiple by COT and true values for the illuminating and shadowy pixels.

To understand how the retrieval bias in CER and COT contribute the net effects in CER*COT and eventually the LWP estimation, we calculated the difference of the retrieved value and the true value for both COT and CER, and evaluate their contribution to the different of the COT*CER in the first order approximation:

$$\Delta LWP \sim \Delta COT \times CER + \Delta CER \times COT \tag{5.1}$$

Figure 5.8 compares the $\Delta CER \times COT$ and $\Delta COT \times CER$ for the illuminating and shadowy pixels For Illuminating pixel, ΔCOT effects is stronger than ΔCER effects; for shadowy pixel, ΔCER effects is stronger than ΔCOT effects. This explains the reason why LWP is frequently over estimated for both the illuminating and shadowy pixels. For the pixels which have large reflectance values, we may need to evaluate the second order contribution to the

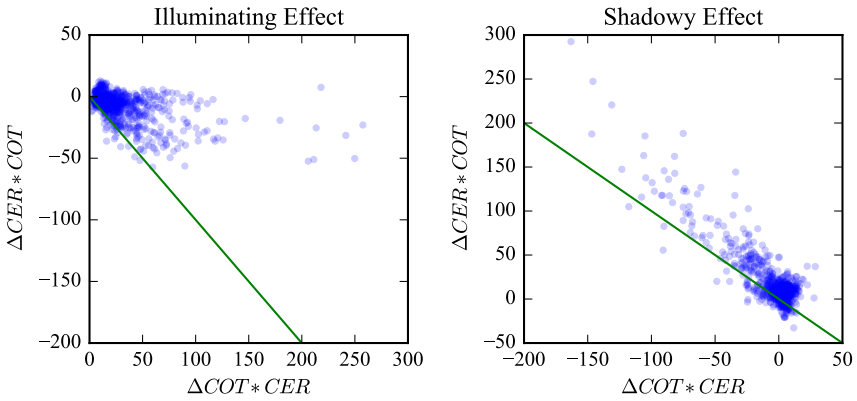

Figure 5.8: The comparison of $\Delta CER \times COT$ and $\Delta COT \times CER$ for the illuminating and shadowy pixels.

changes of the LWP.

6 Conclusions

In this work, we have evaluated the MODIS observations on the low level stratocumulus cloud and studied the fundamental cloud properties including COT and CER. Based on the satellite observations, we generated the surrogate cloud with the same power spectra but different geometric structures using statistical methods. From the studied cloud field, we constructed the cloud structures for both the 3D and 1D radiative transfer simulations and calculated the reflectance at the 0.86μm and 2.1μm bands. The COT and CER are retrieved from the simulated reflectance and compared with the true values. We further evaluated the impact in the retrieval of cloud liquid water path, and find that the bias in the COT and CER will not completely compensate each other but will cause the over estimation of the LWP. Moreover, two different mechanisms are identified for the illuminating and shadowy pixels which shows different changes in the COT and CER but all will cause the over estimation the cloud liquid water path. This work will be beneficial for the correction of the 3D effects in the future satellite product in order to improve the cloud properties retrieval accuracy and global cloud physics studies.

6.1 Future work

This work has many different possible avenues for exploration in the future.

Due to the complexity of the problem that the effects of various factors affecting the radiative transfer intertwine, there is no existing MODIS retrieval method that takes into account the horizontal heterogeneities of the medium. In this regard, existing MODIS atmosphere products are more or less distorted. The previous research on 3D radiative transfer effects based on the MODIS atmosphere products focused on detecting the 3D effects. How

to process the Level 1 product of the MODIS observation data and produce reliable atmosphere products remains an open question.
One line of research can combine the analysis of the retrieval data of MODIS and the simulation study, i.e., use the simulation study to develop methods to eliminate the 3D effects in the retried atmosphere product in the simulated cloud, and then in turn verify the effectiveness by applying them to the retrieval method for processing the Level 1 products MODIS.

Currently, the method to generate 2D surrogate clouds has no known distribution. This could lead to rare event cloud scenes which are not seen in nature. In the future, iterative methods such as [10, 11] could be used to generate surrogate cloud scenes with a Gaussian distribution. A future project would be to study the distribution of the current method and compare it to the distributions of the iterative method and MODIS cloud scenes with similar power spectral densities.

From the cloud scenes in figure 1.1 there are various cloud structures on vastly different scales. In panel (d) of figure 1.1, there are many cloud scenes at the smallest resolution of the MODIS satellite (1km $\times$ 1km). One question to explore is how robust are the results presented here on the resolution of the cloud scene? Before this question can be answered, we must generate surrogate cloud scenes with finer resolution than MODIS.

How do we extend the power spectral density of MODIS to smaller resolutions than MODIS? Two possible methods are discussed here. In figure 6.1, the power spectral density (PSD) of cloud optical thickness (COT) is plotted in panel (a) of a MODIS cloud scene with domain size 50 km by 50 km and resolution of 1 km by 1km. This PSD is then extended to wave numbers of smaller scales (¡1 km, $k_x = k_y = 26...50$) in two different ways. The original PSD is used for scales greater than 1 km, i.e. $k_x = k_y = 0, 1, 2, ..., 25$. For smaller scales, first the PSD is set to zero (panel (b)). This is a quick way to generate surrogate clouds with finer resolutions. However, no additional information is gleaned from these smaller scales. This method is equivalent to taking a 1 km x 1 km pixel and splitting it up into 4, 500 m by 500 m pixels with the same COT value. This method preserves the mean and variance COT of the original scene. Another way of extending the power spectrum is shown in panel (c). Here, the original PSD is used for the larger scales. For the smaller scales, a linear best fit is used on the original power spectrum for wave numbers $\sqrt{k_x^2 + k_y^2} = 4, 5, 6, .., 20$. This captures the general decay of power in a radially symmetric way. The best fit line is used to generate a radially symmetric power spectrum at the smaller scales. This allows for surrogate clouds with finer resolutions which have variations of COT at smaller scales. This results in a cloud scene with the same mean but strictly larger variance of COT as the original.

Further evaluation of the accuracy of the 3D radiative transfer simulation with various spatial resolution in the simulation domain and also evaluate the scale effects by using surrogate cloud with finner structure information beyond 1km resolution used in the current study.

Since we have already generated surrogate cloud with different geometric configurations, we would like to compute the 3D radiative transfer reflectance and evaluate the reflectance difference between different geometries and understand the impacts of the cloud structure in the LWP estimations.

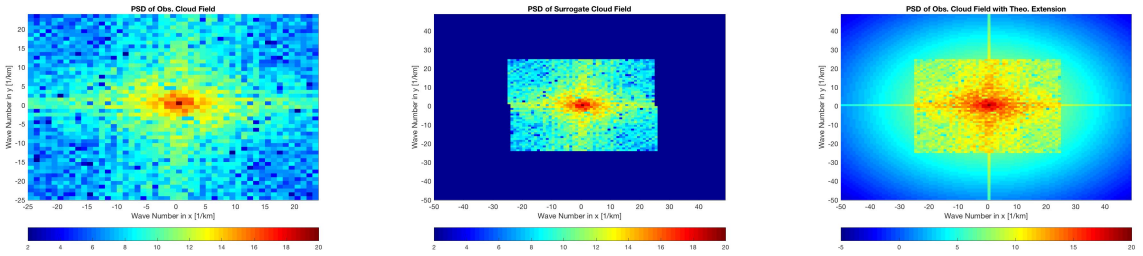

(a) (b) (c)

Figure 6.1: The power spectral density (PSD) for COT for a 50 km by 50 km MODIS cloud scene with (a) 1 km by 1 km resolution. The PSD is extended to a 500 m by 500 m resolution by (b) zeroing out the wave numbers smaller than 1 km, and by (c) doing a linear best fit for wave numbers smaller than 1 km.

Acknowledgments

This work is supported by the grant CyberTraining: DSE: Cross-Training of Researchers in Computing, Applied Mathematics and Atmospheric Sciences using Advanced Cyberinfrastructure Resources from the National Science Foundation (grant no. OAC–1730250). This grant also supported co-author Chamara Rajapakshe as graduate assistant.

The hardware in the UMBC High Performance Computing Facility (HPCF) is supported by the U.S. National Science Foundation through the MRI program (grant nos. CNS–0821258, CNS–1228778, and OAC–1726023) and the SCREMS program (grant no. DMS–0821311), with additional substantial support from the University of Maryland, Baltimore County (UMBC). See hpcf.umbc.edu for more information on HPCF and the projects using its resources.

References

[1] Ákos Horváth C. Seethala. Global assessment of amsre and modis cloud liquid water path retrievals in warm oceanic clouds. *Journal of Geophysical Research*, 115, 2010.

[2] Robert F Cahalan, William Ridgway, Warren J Wiscombe, Thomas L Bell, and Jack B Snider. The albedo of fractal stratocumulus clouds. *Journal of the Atmospheric Sciences*, 51(16):2434–2455, 1994.

[3] Robert F Cahalan and Jack B Snider. Marine stratocumulus structure. *Remote Sensing of Environment*, 28:95–107, 1989.

[4] R. Wood D. P. Grosvenor. The effect of solar zenith angle on modis cloud optical and microphysical retrievals within marine liquid water clouds. *Atmospheric Chemistry and Physics*, 2014.

[5] Robin J Hogan and Anthony J Illingworth. The potential of spaceborne dual-wavelength radar to make global measurements of cirrus clouds. *Journal of Atmospheric and Oceanic Technology*, 16(5):518–531, 1999.

[6] Alexander Marshak, Steven Platnick, Tamás Várnai, Guoyong Wen, and Robert F Cahalan. Impact of three-dimensional radiative effects on satellite retrievals of cloud droplet sizes. *Journal of Geophysical Research: Atmospheres*, 111(D9), 2006.

[7] Teruyuki Nakajima and Michael D. King. Determination of the optical thickness and effective particle radius of clouds from reflected solar radiation measurements. part i: Theory. *Journal of the Atmospheric Sciences*, 47(15):1878–1893, 1990.

[8] Teruyuki Nakajima, Michael D. King, James D. Spinhirne, and Lawrence F. Radke. Determination of the optical thickness and effective particle radius of clouds from reflected solar radiation measurements. part ii: Marine stratocumulus observations. *Journal of the Atmospheric Sciences*, 48(5):728–751, 1991.

[9] Robert Pincus and K. Franklin Evans. Computational cost and accuracy in calculating three-dimensional radiative transfer: Results for new implementations of monte carlo and shdom. *Journal of the Atmospheric Sciences*, 66(10):3131–3146, 2009.

[10] Thomas Schreiber and Andreas Schmitz. Improved surrogate data for nonlinearity tests. *Physical Review Letters*, 77(4):635, 1996.

[11] Thomas Schreiber and Andreas Schmitz. Surrogate time series. *Physica D: Nonlinear Phenomena*, 142(3-4):346–382, 2000.

[12] Samuel N Stechmann and Scott Hottovy. Cloud regimes as phase transitions. *Geophysical Research Letters*, 43(12):6579–6587, 2016.

[13] Alexander Marshak TAMAŚ Várnai. Observations of three-dimensional radiative effects that influence modis cloud optical thickness retrievals. *Journal of the Atmospheric Sciences*, 59, 2002.

[14] Robert Wood. Relationships between optical depth, liquid water path, droplet concentration, and effective radius in adiabatic layer cloud. *University of Washington*, 3, 2006.

[15] Graham Feingold Steven Platnick Robert Pincus Huiwen Xue Zhibo Zhang, Andrew S. Ackerman. Effects of cloud horizontal inhomogeneity and drizzle on remote sensing of cloud droplet effective radius: Case studies based on large-eddy simulations.